Highly textured boron/nitrogen co-doped TiO2 with honeycomb structure showing enhanced visible-light photoelectrocatalytic activity

Amr Nada, Waleed M.A. El Rouby, Maged Bekheet, Manuel Antuch, Matthieu Weber, Philippe Miele, Roman Viter, Stephanie Roualdes, Pierre Millet, Mikhael Bechelany

Highly textured boron/nitrogen co-doped TiO₂ with honeycomb structure showing enhanced visible-light photoelectrocatalytic activity

Amr A. Nada[a,b,*], **Waleed M.A. El Rouby**[c,d], **Maged F. Bekheet**[e] , **Manuel Antuch**[c], **Matthieu Weber**[b], **Philippe Miele**[b], **Roman Viter**[f,g], **Stéphanie Roualdes**[b], **Pierre Millet**[c], **Mikhael Bechelany** [b,*].

[a] Dept. of Analysis and Evaluation, Egyptian Petroleum Research Institute, Cairo, Nasr city P.B. 11727, Egypt.

[b] Institut Européen des Membranes IEM, UMR 5635, ENSCM, Université de Montpellier, CNRS, Place Eugène Bataillon, CC047, F-34095 Montpellier Cedex 5, France.

[c] Paris-Sud University, ICMMO-Eriée, UMR CNRS 8182, 91405 Orsay, France.

[d] Materials Science and Nanotechnology Department, Faculty of Postgraduate Studies for Advanced Science (PSAS), Beni-Suef University, 62511 Beni-Suef, Egypt.

[e] Fachgebiet Keramische Werkstoffe / Chair of Advanced Ceramic Materials, Institut für Werkstoffwissenschaften und -technologien, Technische Universität Berlin, Hardenbergstraße 40, 10623 Berlin, Germany

[f] Institute of Atomic Physics and Spectroscopy, University of Latvia, 19 Raina Blvd., LV 1586 Riga, Latvia

[g] Sumy State University, Center for Collective Use of Scientific Equipment 31, Sanatornaya st., 40018, Sumy, Ukraine.

∗ Corresponding authors.

E-mail address: mikhael.bechelany@umontpellier.fr (M. Bechelany).

amr.nada@umontpellier.fr (A. A. Nada)

In this work, we report a novel photocatalyst based on boron and nitrogen co-doped TiO_2 rutile (110) honeycomb structures. The photocatalyst has been prepared by simultaneously oxidizing and doping a Ti-foil substrate at 750°C. The unit cell volume and the crystallite size of grown TiO_2 films were measured by Rietveld refinement analysis. The co-doping by boron and nitrogen was achieved simultaneously with the oxidation of the titanium, resulting in a rutile (110) textured TiO_2 film. X-ray photoelectron spectroscopy analysis revealed the presence of Ti-O-N and Ti-O-B-N bonds, and the presence of crystal defects in the lattice was detected and displayed by Raman spectroscopy. The water photo-oxidation properties have been measured as well, and the photocurrent of the B/N co-doped rutile sample prepared reached 270 µA/cm^2 at 1V under visible light and was stable in time. The efficient visible light absorption properties of the fabricated nanomaterial were attributed to the presence of oxygen vacancies and the introduction of impurity levels, as well as to synergistic effects between the introduced boron and nitrogen elements. The results presented demonstrate a new route for the preparation of TiO_2 based catalysts, and open prospects for the photocatalysis community.

Introduction

Hydrogen is considered to become an upcoming and key energy vector in the near-future, and considerable efforts are currently undertaken to develop and optimize the different technologies required for the implementation of a hydrogen economy[1,2]. In this context, water photo-dissociation is a topic of great technical potential. Different semiconductors have been used so far to perform water splitting, for example MoS_2, WO_3, CdS, Fe_2O_3 and TiO_2 [1,3–7]. Among them, TiO_2 is probably the most popular for water photo-oxidation. In fact, this material presents the necessary chemical stability for oxygen evolution in aqueous media, is inexpensive and environmentally friendly [8–10]. However, the band gap of TiO_2 is too wide and cannot absorb visible light. Therefore, different approaches have been proposed to shift absorption of this material to the visible range: coupling with another semiconductor [11,12], addition of photosensitizers [13–15] or co-catalyst [9,16–18], doping with transition metals or lanthanide [1,19–21] and doping with non-metallic elements such as C, S, B and N [22–24]. The doping of TiO_2 with non-metallic elements is a very promising route to tune the optical properties of this material. Such doping does not only shift the absorption edge to the visible region but also enables to improve the electron/hole stability [25–27]. In addition, the introduction of B and N dopants can trigger higher photo-electrocatalytic performance, and the photoactivity of these materials strongly depends on their crystallinity. Different photoactivities have been reported, for example for undoped and n-type doped TiO_2 rutile single (100) and (110) crystals [28].

It has been shown that TiO_2 nanomaterials co-doped with boron and nitrogen (B/N) have shown enhanced photocatalytic activity and stability under visible light irradiation, which was attributed to synergistic effects between boron and nitrogen [29]. According to literature, the photocatalytic activity of boron-doped TiO_2 strongly depends on the fabrication process [23]. In contrast, the nitrogen-doped TiO_2 was found to improve the photocatalytic activity

independently of manufacturing conditions. However, it has also been reported that nitrogen could adsorb only at the surface of TiO_2, and this can reduce the photo-activity [30].

Regarding the preparation methods, polycrystalline B/N co-doped TiO_2 nanomaterials have been prepared using different techniques such as sol-gel [31–33], hydrothermal [34–36] and aerosol-assisted flow synthetic method [37]. But so far, there is no report on the influence of B/N co-doping rutile TiO_2 (110) for the photocatalytic activity.

The objective of this work is to elaborate B/N co-doped TiO_2 rutile and to investigate its water photo-oxidation properties. The growth of the (110)- textured material, B/N co-doped TiO_2 rutile, was achieved using a simultaneous oxidising and doping process, using pulses of BBr_3 and ammonia at high temperature. The morphology of the grown films has been tuned by varying the pulses times, and a honeycomb structure could also be formed under specific conditions. The technique has been applied to elaborate such materials and this specific B/N co-doped TiO_2 rutile with (110) texture and honeycomb structure was obtained for the first time. The structure, the morphology, as well as the optical properties of the elaborated nanomaterials were measured and discussed. The photo-electrocatalytic activity with regard to water photo-oxidation into molecular oxygen under visible light irradiation. Also, the reaction mechanisms have been discussed, based on photo-electrochemical impedance spectroscopy data.

Experimental section

   1. **Chemicals and materials**

Boron tribromide 99.9% (CAS number: 10294-33-4), Ti foil 99.99% - 025 mm thick (CAS number: 7440-32-6) and Sodium sulphate 99.99% (CAS number: 7757-82-6) were purchased

from Sigma Aldrich, and used without any further purification. The ammonia gas (99.96% purity with 0.04% water as main impurity) was purchased from Linde company.

2. Oxidation and B-N co-doping of titania films

All samples were synthesized in a vacuum system, described elsewhere [38]. The initial Ti foil substrates were placed under a base pressure of 1.10^{-2} mbar. The 2 cm^2 of Ti- foils samples were pre-cleaned in ethanol for 10 min in an ultrasonic bath before the process. The simultaneous oxidising and doping was carried out by pulsing Boron tribromide (BBr$_3$) for the B doping and ammonia for the N doping in this vacuum system at 750°C. The pulses were 30s long. Different samples have been prepared, where the number of B and N pulses was varied: 65, 125 and 250 pulses of both BBr3 and ammonia have been carried. The corresponding samples are referred to as BN65, BN125 and BN250, respectively. In addition, a sample with only NH$_3$ pulses has been prepared (referred as N125) without exposure to BBr$_3$ for comparison.

3. Material characterizations

The crystallinity of the prepared thin films was analysed using X-ray diffraction (XRD) with a PANAlytical Xpert-PRO diffractometer equipped with an Xcelerator detector and using a Ni-filtered Cu-radiation (CuKα1 radiation wavelength 0.1540598 nm and CuKα2 radiation wavelength 0.1544426 nm). The scan step size was fixed to 0.0167 degree/step and the time per step was set to 0.55 sec/step. Rietveld refinement was performed using the FULLPROF program [39] and profile function 7 (Thompson-Cox-Hastings pseudo-Voigt convoluted with axial divergence asymmetry function) [40]. The resolution function of the instrument was obtained from the structure refinement of silicon standard. More information about using

pseudo-Voigt function to calculate the crystallite size and micro-strain is reported elsewhere [41]. The elemental composition on the surface of the grown thin films were determined by X-ray photoelectron spectroscopy (XPS) on an Escalab 250 (Thermo Fisher Scientific, USA) using a monochromatic Al K Alpha (1486.6 eV) at 2kV and 1 µA. Raman spectra were measured on a Horiba XploRA, λ= 659 nm at a power of 20 W and a microscope objective lens of 100x. The morphology of the grown thin films was put in evidence by using a Hitachi S4800 (Japan) scanning electron microscope (SEM). The optical band gap of the samples was determined from experimental UV-Vis spectra. These spectra were measured on a Jasco (model V-570) UV-Vis spectrophotometer equipped with a diffuse reflectance (DR) device (Shimadzu IRS-2200).

4. Photoelectrochemical measurements

A conventional photoelectrochemical three-electrode cell equipped with a quartz window (Pine Research Co., USA) was used for the photoelectrochemical experiments. The B/N co-doped TiO_2 (110) samples were used as working photo-anodes. A Pt wire and a saturated calomel electrode (SCE) were used as counter and reference electrodes, respectively. In all measurements, a 0.1 M aqueous solution of $NaSO_4$ (pH~6.5) was used as electrolyte. The electrolyte was purged with Argon for 30 min and an Argon cloud was kept over the electrolyte during the whole experiments. Measurements have been made using a ModuLap XM potentiostat (Solartron Analytical, USA). The photocurrent-potential curves were measured by scanning the potential of the working electrodes from the 0.0 V/SCE to 1.1 V/SCE at a scan rate of 10 mV.s^{-1}, under dark and illumination conditions. The working photo-anode was irradiated using a solar simulator (Asahi spectra, MAX-303, USA) equipped with a 300 W Xenon lamp coupled with an air mass 1.5 global filter and a UV cut-off filter (>400 nm). The light source was placed away from the working electrode at a

distance such that a power density of 63 mW cm^{-2} was used. Photoelectrochemical impedance spectra (PEIS) were measured with and without a UV cut filter and under dark condition at different potentials (from -0.6 to 1.2 V/SCE), over the frequency range of 100 kHz – 50 mHz, using an AC voltage of 10 mV amplitude.

Results and discussion

All samples were prepared at 750°C in a vacuum system. The initial Ti foil substrates were submitted to simultaneous oxidising and doping process, by exposing the samples to a boron precursor (BBr$_3$) for the B doping and to ammonia for the N doping at 750°C. The pulse exposures were 30s long, and 65, 125 and 250 pulses of BBr$_3$ and of NH$_3$ were applied to obtain the samples referred as BN65, BN125 and BN250. The oxidation process of Ti to TiO$_2$ may seem surprising at first, as no oxygen per say was inserted in the reactor. However, the conversion to TiO$_2$ has been observed and explained by the remaining oxygen species in the ammonia container. In fact, Ti presents a high susceptibility to oxygen at such high temperatures, enabling the oxidation to take place and successfully convert the Ti to crystalline TiO$_2$ material, in parallel to the B and N doping process. The properties of the B/N co-doped TiO$_2$ samples were then investigated. Firstly, the XRD patterns measured on the different doped TiO$_2$ films are presented in Figure 1.
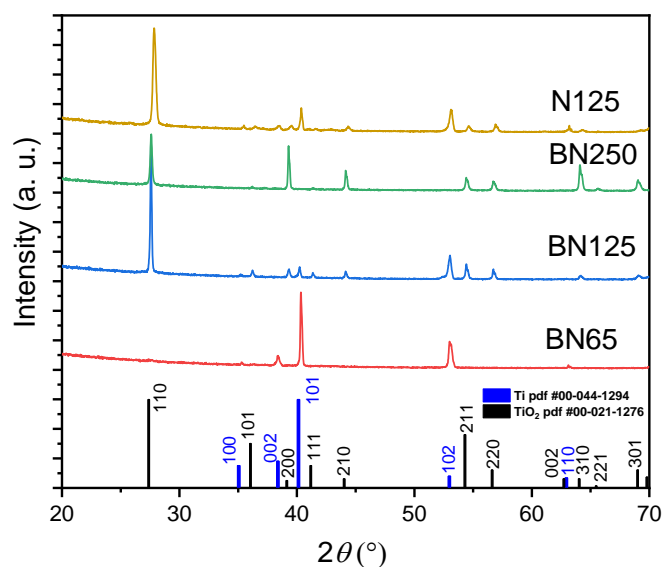
Figure 1: XRD patterns of BN65, BN125, BN250 and N125 samples. The calculated patterns of Ti metal (PDF Card #00-044-1294) and rutile TiO_2 (PDF Card #00-021-1276) are shown at the bottom of the figure.

All the peaks appearing on the XRD patterns can be indexed to the rutile phase of TiO_2 (PDF Card #00-021-1276) and no other phase of TiO_2 has been observed. It can be seen that the intensities of the XRD reflections corresponding to the TiO_2 phase are very low for the sample BN65 as presented in Figure S1, indicating the small percentage of TiO_2 film on the surface of the Ti substrate. In contrast, no XRD reflections corresponding to Ti substrate were observed in the pattern of the BN250 film prepared after 250 pulses. This is due to the large thickness of the TiO_2 film obtained after such a long exposure to the oxidising/doping process. A comparison of the intensities of XRD reflections belonging to the TiO_2 phase, in each film and with those calculated for the reference rutile TiO_2 phase (PDF Card #00-021-1276), suggests a preferred orientation along the [110] direction in the BN125 and N125 films prepared in presence or absence of boron, respectively. The preferred orientation

changes in BN250 film to the [200], [210] and [310] directions as the number of pulses increased.

To gain further insight about the lattice parameters, crystallite size, microstrain and preferred orientation of the samples, a Rietveld refinement was performed on the diffraction patterns using the FULLPROF program [39] with the profile function 7 (Thompson-Cox-Hastings pseudo-Voigt convoluted with axial divergence asymmetry function) [40]. The preferred orientation was determined with the March-Dollase model [42], as implemented in the FULLPROF program. It is worth to note here that it was difficult to refine crystallite size, microstrain and preferred orientation for BN65 sample due to the low intensities of its XRD reflections. Figures 2-A to 2-D show the observed, calculated and the difference profile for the final cycle of the structure refinement. The results of Rietveld refinement are compiled in Table 1. The lattice parameters and unit cell volume of the rutile TiO_2 phase in all doped samples are slightly higher than those reported previously to the undoped rutile TiO_2 (a = 4.5933 Å, c = 2.9592 Å and cell volume = 62.43 Å^3, PDF Card #00-021-1276), which suggests the incorporation of B/N in the interstitial sites and/or the generation of oxygen vacancies inside the TiO_2 lattice. The increase in the unit cell volume of TiO_2 due to the oxygen vacancies in its lattice can be explained by the valence decrease of Ti ions from +4 to +3 as the charge compensation (ionic size of Ti^{+3} is larger than that of Ti^{+4}). The generation of oxygen vacancies in the grown TiO_2 films was further confirmed by XPS characterization as discussed below. However, the lattice parameters and unit cell volume of the rutile TiO_2 phase do not change with increasing the duration of the oxidizing/doping process, which indicates that the highest amount of B/N co-doping into the TiO_2 lattice can be achieved with low cycle of deposition (65 pulses). These results reveal that the BN125 and BN250 films have oxygen vacancies.

In contrast, the size of TiO_2 crystallites increases with the B/N co-doping, whereas the microstrain decreases. The March-Dollase (MD) parameter r along the [110] direction was found to be 0.47(1) and 0.53(1) in the N125 and BN125 sample, respectively. This MD parameter r define the distribution shape of the crystallites and is being unity for an ideal random-orientation (i.e. no preferred orientation), greater than one for needle-habit crystals and less than one for platy crystals pack along the diffraction vector. Thus, the TiO_2 crystals are grown as plats along the [110] direction in both N125 and BN125 samples, suggesting that B/N co-doping does not change the habits of TiO_2 crystals as well as the growth direction.
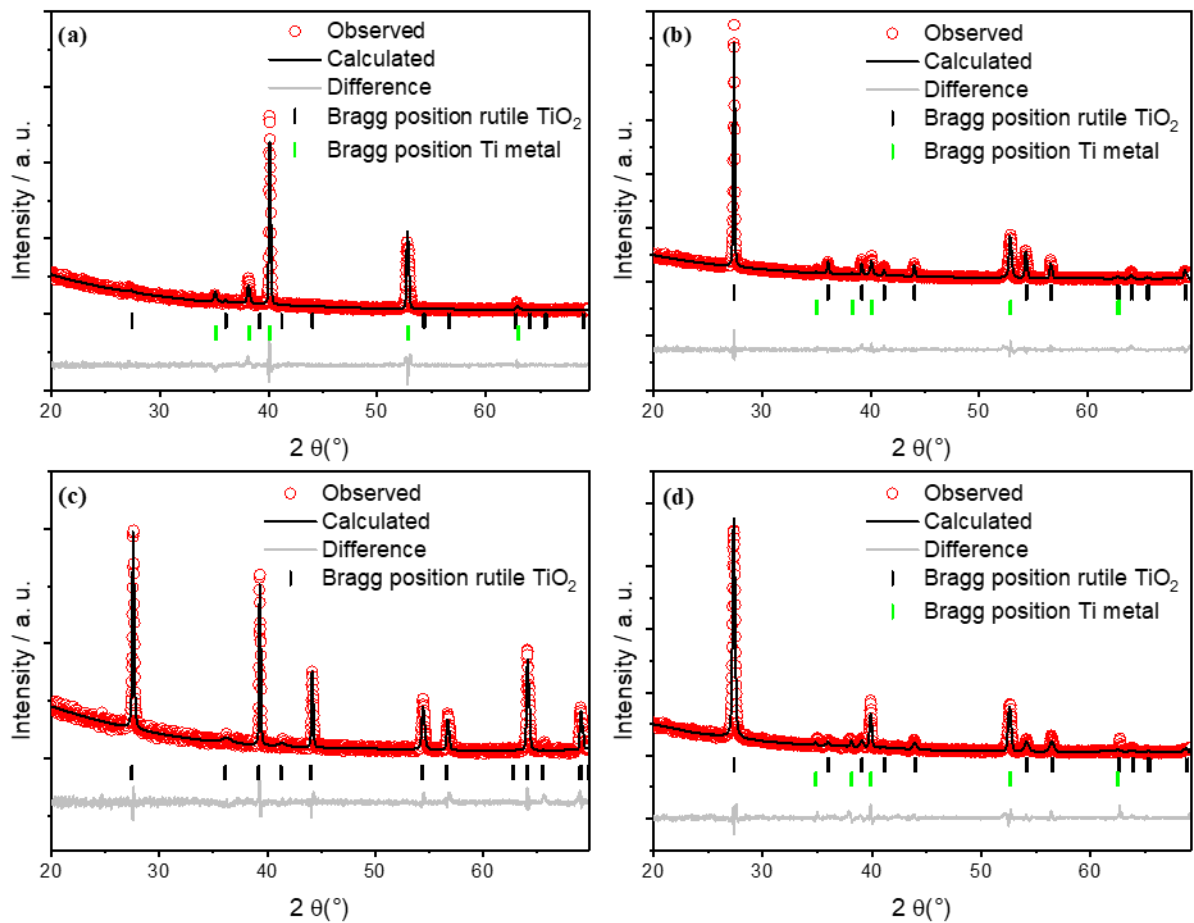
Figure 2: Structure refinement of X-ray powder diffraction data collected at room temperature for BN65 (A) and BN125 (B), BN250 (C) and N125 (D) samples showing the observed (red circle) and calculated (black solid line) intensities, the calculated Bragg reflections (tick marks), and the difference (grey solid line).

However, the degree of the preferred orientation η along the [110] direction, which is calculated from MD parameter r using the Zolotoyabko equation [43], was found to be 34.9% in BN125 sample that is slightly lower than that in N125 sample (e.g. 40.8%). η indicates the percentage of excess of crystallites with preferential orientation in comparison with randomly oriented crystallites in the film, which means that N125 sample has crystallites with preferential orientation along the [110] direction more than those in the BN125 sample. On the other hand, the increase of the duration of the oxidising/doping process in the presence of B/N as co-dopants led to the change in the preferred orientation changes from [110] direction to the [200], [210] and [310] directions as found for the BN250 film. Previous theoretical and experimental works reported that the average surface energy of the (110) crystal planes of rutile TiO_2 is lower than those of (100) and (210) planes [44–46]. Therefore, rutile TiO_2 crystals is preferential to grow along [110] direction, where (110) planes are most thermodynamically stable due to their low surface energy. However, recent study showed that the strain energy of TiO_2 crystallites in the polycrystalline films could also control the direction of the crystal growth and the competition between surface energy and strain energy during film growth might change the direction of the texture [47]. As shown in Table 1 and Figures 1 and 2, the [110] texture in the N125 and BN125 samples is accompanied with high microstrain and low film thickness as the XRD reflections of Ti substrate are still observed in the XRD pattern. In contrast, the [200], [210] and [310] textures were observed for BN250 film that has the lowest microstrain and highest thickness. Previous work showed that the

surface and interface energy minimizing textures are found in very thin films, while, strain energy minimizing textures are favored for thicker films [48]. Accordingly, these results indicate that the [110] texture for rutile TiO_2 is dominated by surface energy minimization, while, the [200], [210] and [310] textures is dominated by strain energy minimization in the growth process.

Table 1: A summary of structural parameters extracted from the XRD patterns by Rietveld refinement of N10, BN5, BN10 and BN20 samples: lattice parameters a, b, c [Å], the unit cell volume V [Å^3], crystallite size [nm] and Microstrain and preferred orientation parameters obtained from March-Dollase (MD) model. r, f and η are March-Dollase parameter, the fraction of crystallites that are associated with a particular orientation axis and degree of preferred orientaion, respectively.

Sample	Lattice parameter (Å)	Unit cell volume (Å³)	Crys. size (nm)	Micro-strain x 10⁻³	Preferred orientation parameters			
					(hkl)	$r_{(hkl)}$	$f_{(hkl)}$	$\eta_{<hkl>}$
N125	$a = 4.5975(7)$ $c = 2.9613(9)$	62.59(2)	67.9(1)	3.2(2)	(110)	0.47(1)	1.0	40.8
BN65	$a = 4.5991(8)$ $c = 2.9632(8)$	62.68(1)	-	-	-	-	-	
BN125	$a = 4.5985(3)$ $c = 2.9609(3)$	62.61(2)	>100	1.1(1)	(110)	0.53(1)	1.0	34.9
BN250	$a = 4.5996(4)$ $c = 2.9614(3)$	62.65(1)	89.9(1)	0.8(1)	(200) (210)	0.38(1) 0.25(1)	0.72 0.15	36.1 9.8

					(310)	0.24(2)	0.13	8.7

In order to determine the chemical composition of the samples after the oxidising/doping treatment, the BN125, BN250 and N125 samples have been analysed by X-ray photoelectron spectroscopy (XPS). The XPS spectra of O 1s, Ti 2p, N 1s and B 1S orbitals are shown in Figure 3 a-d. The spectrum of O 1s (Figure 3-a) contains a main peak at ~529.9 eV identical to the oxygen in rutile lattice (O_{latt}) and another peak at 531.3 eV corresponding to the surface adsorbed oxygen ($O_{ads.}$) [1]. The amount of surface oxygen vacancies can be estimated by the ratios between O_{ads} to O_{latt}. The higher ratio refers to an enrichment of surface oxygen vacancies. The O_{ads}/O_{latt} ratios were found to decrease by increasing the dopants exposures: 0.77, 0.71 and 0.52 for BN125, BN250 and N125, respectively. Boron and nitrogen co-doping introduced more oxygen vacancies inside the titanium lattice than nitrogen-doping alone, with the same number of B and N precursor pulses (~ 0.25). The same conclusion is reached by analysing the XPS doublet peak $Ti2p_{3/2}$ and $Ti2p_{1/2}$ (Figure 3b) located at about 459 and 464.8 eV, respectively for N125. These peaks have the characteristic binding energies of Ti^{4+} in the TiO_2 rutile matrix [49]. The Ti 2p peaks are shifted to lower binding energies by about ~0.3 eV for BN125: this suggests the presence of nitrogen and boron in the TiO_2 lattice. The lower shift of Ti 2p peaks referred to the replacement of oxygen (highly electronegativity) by lower electronegativity boron and nitrogen. In addition, the N 1s peaks of the samples (Figure 3c) can be fitted to three peaks at ~ 396, 400 and 402 eV, corresponding to substitutional nitrogen (Ti-N; N1), interstitial nitrogen (Ti-O-N or Ti-O-B-N; N2) and chemisorbed N_2 (N3), respectively [50,51]. The ratio of the N3 to (N1+N2) peaks is increased 4 times for BN125 compared to N125. This refer to the amount of doped substitutional and interstitial N ions that they were decreased in case doping with B and N,

and the chemisorbed N_2 that they were increased compared to N doped only in the same number of pulses. In addition, the ratio of adsorbed nitrogen in BN125 was found to be 1.5 times larger than in BN250.

In contrast, the B 1s peak fitting of BN125 and BN250 was been presented in Figure 3d. In the case of BN125, the fitting of B 1s was observed at 190.6 and 192.1 eV corresponding to the formation of Ti-O-B and boron oxide (B-O), respectively [30]. In addition, the ratio between B doped in titanium lattice to B in boron oxide was 3.2 in BN125 and this ratio was decreased 10 times in case of BN250. The increase of the number of pulses led to the formation of a boron surface outer the titanium lattice. In addition, the expected peaks at 189.9-190.2 eV (B 1s) and 398 eV (N 1s) corresponding to BN were not observed.

From XPS, the doping of boron and nitrogen of rutile were favourable in the case of single orientation (as observed in sample BN125) than different orientations (as observed in samples BN250) for the used amount of boron and nitrogen.
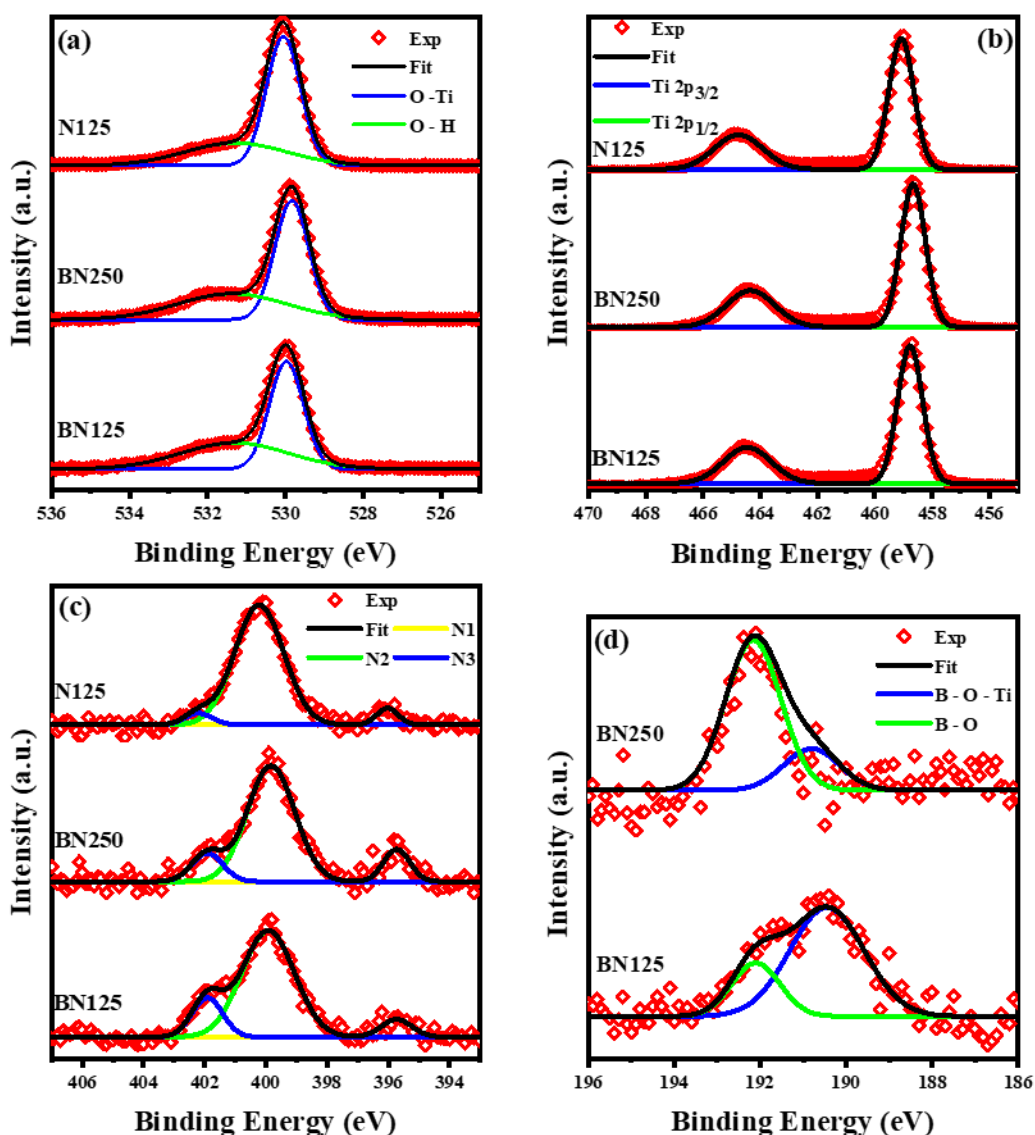
Figure 3. High-resolution XPS spectra of O1s (a), Ti2p (b), N1s (c) and B1s for BN125, BN250 and N125 samples.

The results and conclusions obtained by XPS analysis were confirmed by Raman spectroscopy analysis. Results are reported in Figure 4. Typical Raman active modes of TiO_2 rutile phase are observed for N125, BN125 and BN250 samples. The E_g mode related to oxygen displacements along the c-axis in un-doped TiO_2 rutile (D_{2h}^{14}P4/mnm) is observed at 450 to 449 cm^{-1} [52,53]. For N125, BN125 and BN250 samples, the E_g mode was shifted by

$\approx$ 6, 16 and 8 cm^{-1}, respectively. These shifts reveal the formation of the Ti–O–N for N125 and Ti–O–N–B bonds for BN125 samples [54]. The amount of boron inside the TiO$_2$ rutile phase is less for BN250 than for BN125, as confirmed by XPS analysis, and this is attributed to the formation of B-O bond. Furthermore, an E_g/A_{1g} internal ratio of 1.34 and 1.50 was recorded for BN125 and N125, respectively. This decrease was very sensitive and related to the decrease of oxygen vacancies in the TiO$_2$ rutile after doping with boron and nitrogen [55]. In addition, no significant peak that could be attributed to the BN bond (in the 1300-1500 cm^{-1} range of the Raman spectra) was experimentally observed [1]. This observation leads us to the conclusion that no BN phase was formed.
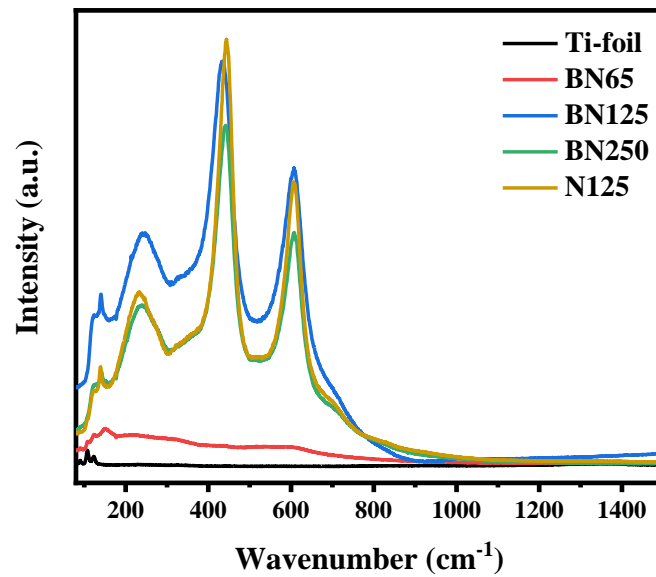

Figure 4: Raman spectra of all samples Ti-foil, BN65, BN125, BN250 and N125

The morphology of the B/N co-doped TiO$_2$ rutile thin films obtained was investigated by SEM. The SEM images are reported in Figure 5. As can be seen in Figures 5-a and 5-b, the BN65 film presents a mixture of small spherical particles. The TiO$_2$ rutile obtained for the samples BN125 and N125 present a plat-like morphology with preferred orientation along

specific directions (Figures 5-c to 5-h). In particular, a honeycomb pore structure was observed in the presence of boron (BN125, Figures 5-c and 5-d). The inorganic honeycomb pores observed on the BN125 sample have a regular size and a diameter of 3.4±0.4 µm. The plat-like growth of TiO_2 crystals along the [110] direction in the N125 and BN125 films was also confirmed by Rietveld refinement analysis of XRD results. The TiO_2 rutile crystals observed on BN250 have a non-homogeneous shape due to the growth along several orientation (Figure 5-e and 5-f), which agrees with the XRD results (Figure 2c and Table 1).

The formation of boron oxide on sample BN250 prevents the formation of the honeycomb structure observed on BN125. The different morphologies obtained when increasing the duration of the oxidation/doping process are likely to be due to growth in one orientation as calculated by the March-Dollase (MD) parameter. it was less than one in the case of BN125 and N125. The crystals are grown as plats along the [110] direction. The thicknesses of the oxidised/doped layers have been estimated as well for the BN65, BN125, BN250 and N125, as extracted from the SEM cross-sections observation (see inset of Figures 5-a, 5-c, 5-e and 5-g). Values of 0.4, 1.1, 2.0 and 1.0 µm were estimated, respectively. As expected, the sample thickness increased with the number of pulses, corresponding to the oxidation (and added elements). The thicknesses of samples BN125 and N125 are very close to each other.
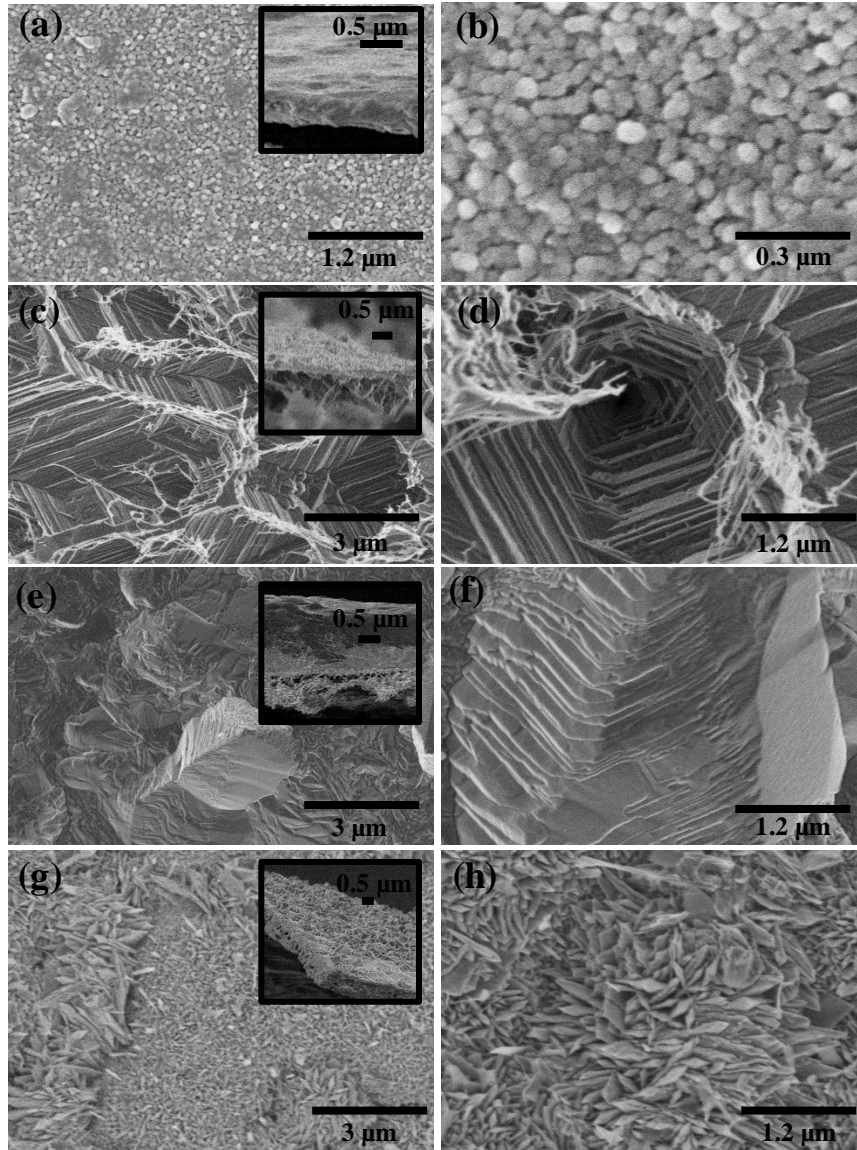
Figure 5: Scanning electron microscope images of BN65 (a and b), BN125 (c and d), BN250 (e and f) and N125 (g and h) samples. Cross Section of BN65, BN125, BN250 and N125 (insets in a, c, e and g ,respectively).

For band gap calculation of BN125 and TiO$_2$-NN125 samples, the measured reflectance spectra were converted into absorption spectra by using the following equation, related to diffuse reflection [1,8]:

$$F = \frac{(1-R)^2}{2 \cdot R} \quad \text{equation (1)}$$

where F and R are Kubelka–Munk function and reflectance, respectively. The band gap of BN125 and N125 samples was calculated as following [1,8]:

$$(F \cdot hv)^{\frac{1}{2}} \sim (hv - E_g) \quad \text{equation (2)}$$

where hv and E_g are photon energy and band gap. The E_g values were obtained as intersection of linear part of the plot at point F=0 (Figure 6).

The obtained values were 2.5, 2.6 and 2.77 eV for N125, BN125 and BN250, respectively. The band gap of the other sample (BN65) was difficult to detect due to low thickness of the TiO$_2$ layer. The obtained values are significantly lower than the band gap of bulk rutile titania (3.05 eV) [56]. We suppose that due to B- and/or N- doping, red shift of the band gap took place. The observed results are in good correlation with results reported by Ansari *et al.* and Surah *et al.* [57,58].
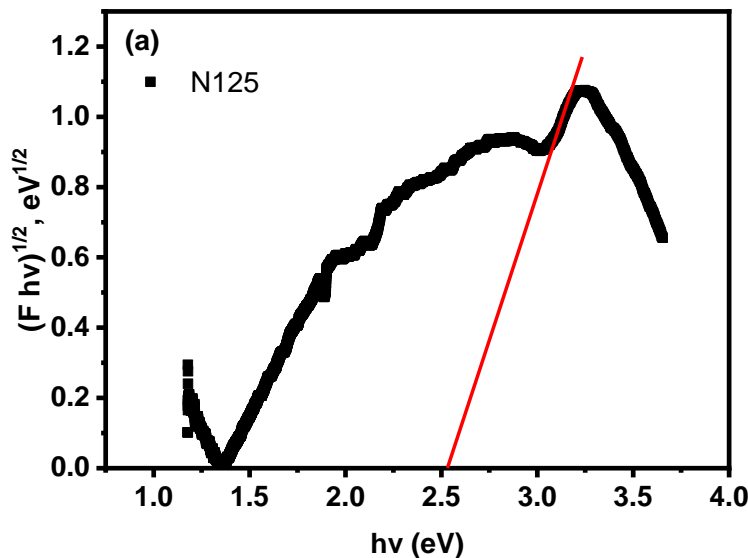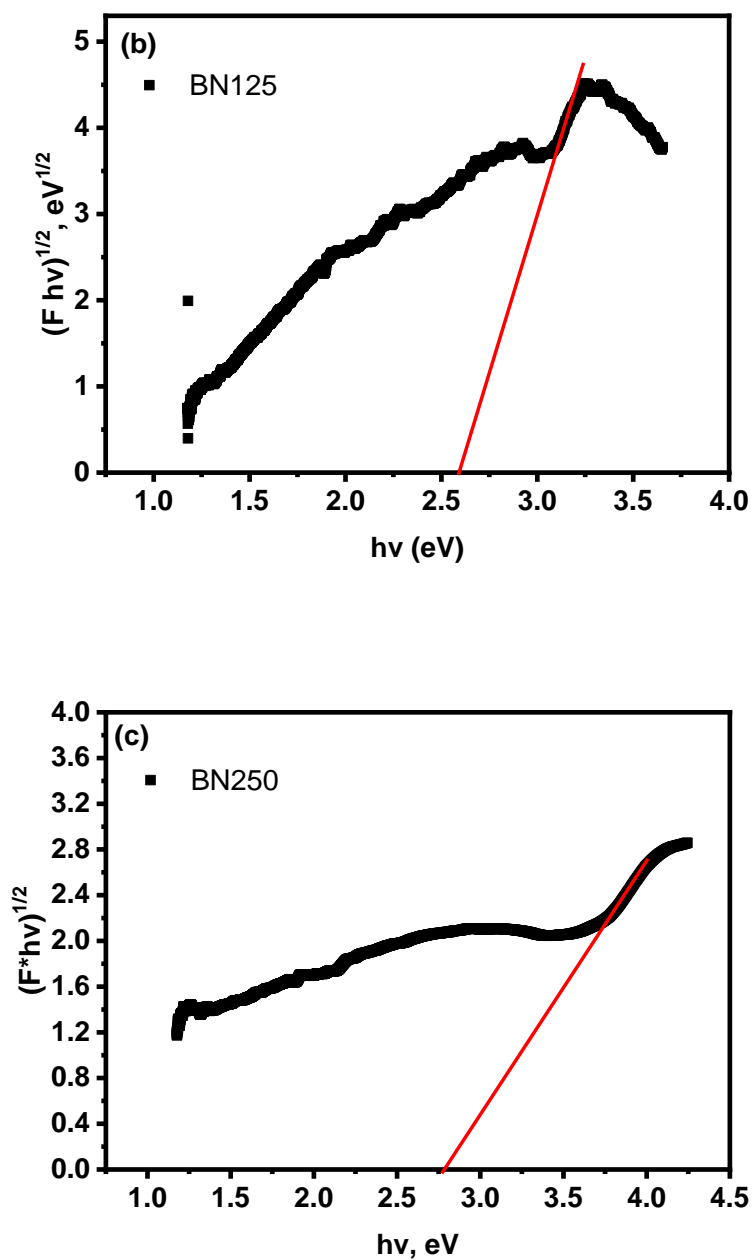
Figure 6: Band gap spectra of (a) N125, (b) BN125 and (c) BN250 samples.

Photoelectrochemistry

The ability of the prepared B and N co-doped TiO_2 samples to split water under external positive potential bias has been investigated using linear sweep voltammetry under chopped illumination conditions (Figure 7-a). The positive photocurrent recorded during the

experiments clearly demonstrates the n-type conductivity of the doped TiO_2 material. Interestingly, the highest photocurrent was obtained for the BN125 sample, and the lowest photocurrent was displayed by the BN250 sample. Figure 7-b shows the results measured during chronoamperometry experiments at a constant operating potential of 1.0 V/SCE and under chopped illumination conditions. It can be noted that the current spikes observed at the onset of the potential are of small amplitude: this is an indication that charge recombination is very limited. Figure 7-c shows the results of chonoamperometry experiments performed over one hour at a constant potential of 1.0 V/SCE, under constant light irradiation conditions. After an approximate 10% reduction of the initial current density for the first 10 minutes, a stable current density was obtained for all samples, indicating a good chemical stability for water splitting under such experimental conditions.

The photocurrent activity obtained is this work exceeds most of the photocurrent activity of nanostructured TiO_2 photoelectrodes doped with N, S or B reported in the literature when illumination under visible light as presented in Table 2 [51,59–62].
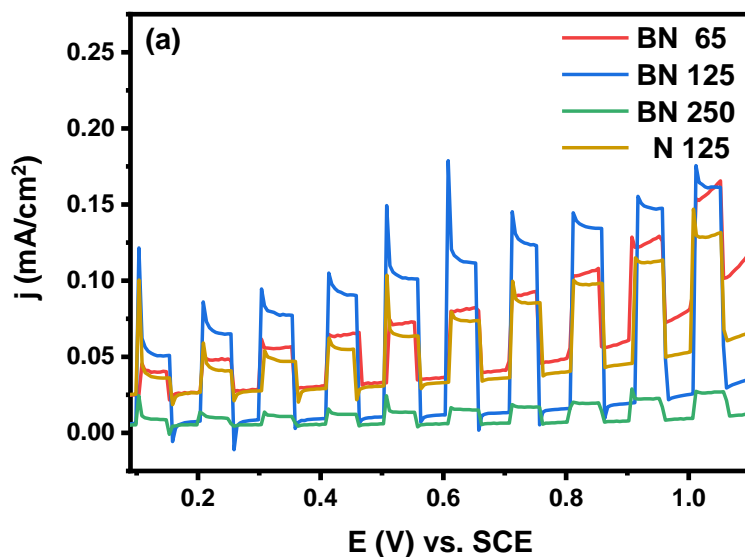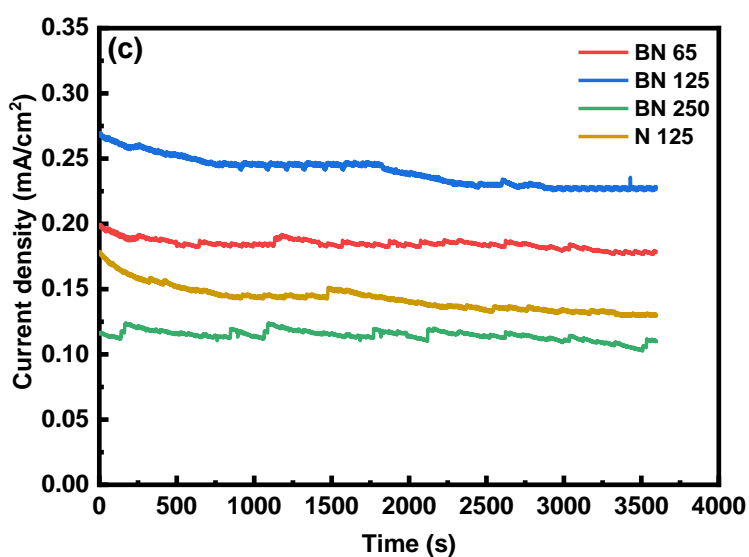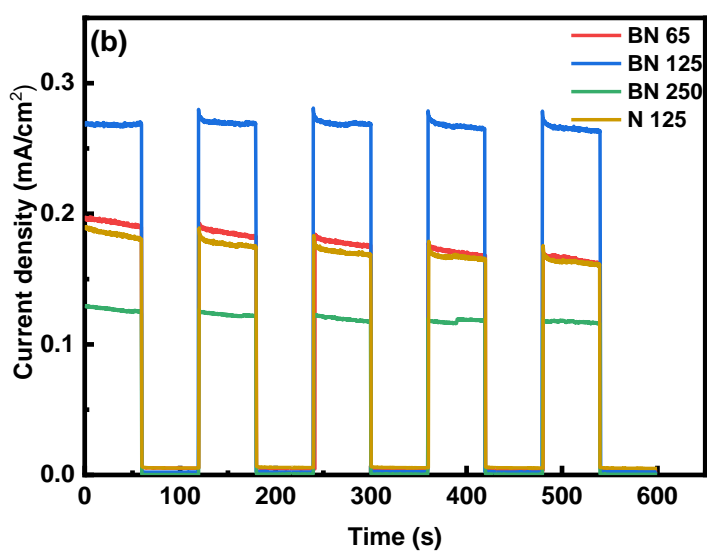
Figure 7. (a) Linear sweep voltammograms measured on the photoelectrodes; (b) potentiostatic plots at 1 V/SCE; (c) Stability tests at 1.0 V/SCE.

Table 2. Maximum photocurrent activity of various B/TiO$_2$ and N/TiO$_2$ photoelectrodes.

Sample name	Photocurrent	Light source	References

	density ($\mu A/cm^2$)		
$TiO_{2-x}N_x$ film	150 at 1V	A sulfur lamp with intensity close to 300 W	[59]
N+S-doped TiO_2 nanotube	28 at 0.2V	A xenon lamp 300W	[60]
B doped TiO_2 nanotube	20 at 1V 350 at 1V	A Xe lamp 350W UV light	[61]
B/TiO_2	20 at 1V 270 at 1V	Visible light (Xe lamp 500W) UV light	[62]
B/N co-doped TiO_2	150 at 1V	LED light (visible light)	[51]
BN125	270 at 1V	Visible light (Xe lamp 300W)	This work

In order to explain the variation of the photocurrent intensity as a function of potential, and to gain a deeper understanding of the dynamics of charge transfer and recombination at these interfaces, photoelectrochemical impedance spectroscopy (PEIS) was recorded which consists in a typical impedance spectrum at a constant potential and constant light power [63–65]. PEIS spectra were recorded here over a wide potential window under visible-light illumination. Experimental PEIS data were analyzed by using the electrical analogy of Figure 8-a [66–75] with two time constants. In this equivalent circuit, the relevant kinetic information is embodied in the resistances. The model assumes the existence of surface trapping sites. R_{trap}^{CT} is the charge transfer resistance that characterizes the transfer of charge carriers (holes) through the interface to oxidize water into molecular oxygen. The lower the value of R_{trap}^{CT}, the faster the transfer of holes from the electrode to the solution.

(a)

Q_{bulk}

Q_{trap}

R_{trap}

R^{CT}_{trap}

(b)

- BN 65
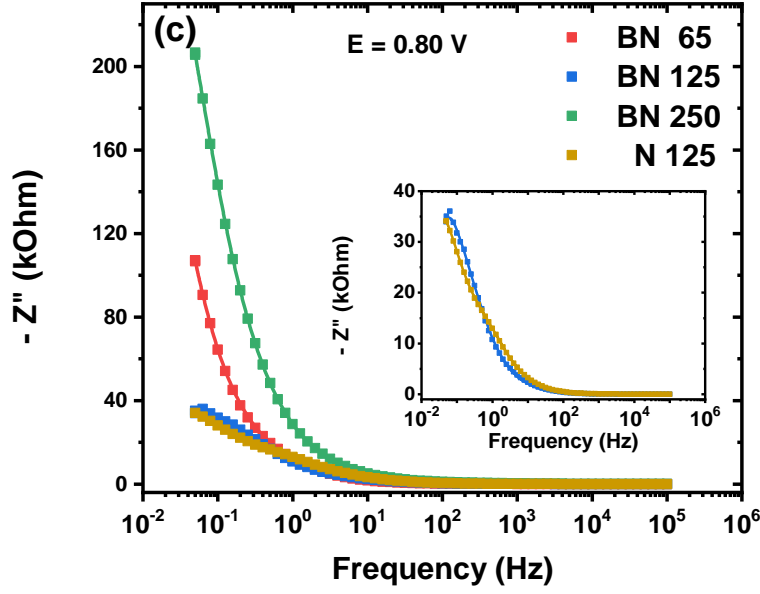- BN 125
- BN 250
- N 125

E = 0.80 V
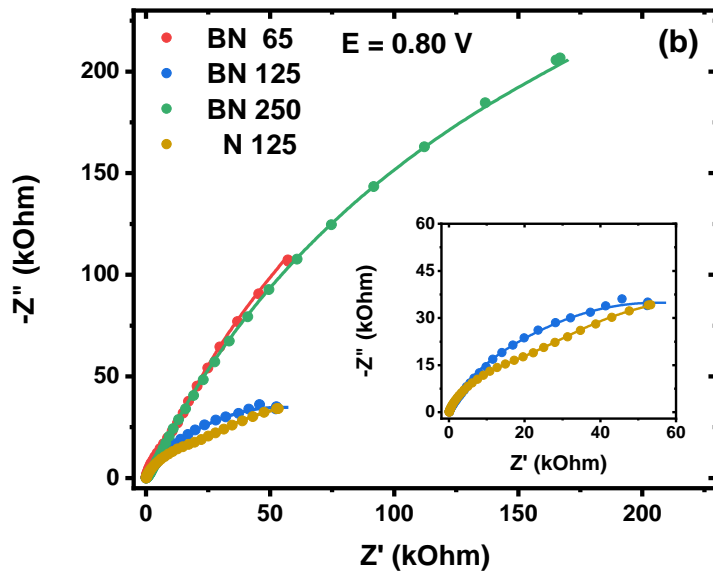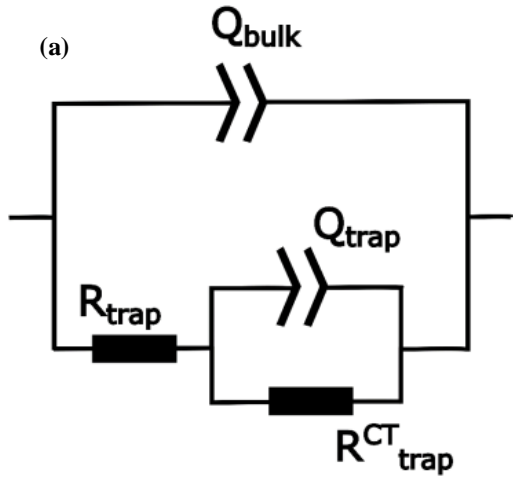
Figure 8. (a) equivalent circuit used to model impedance data (b) typical photoelectrochemical impedance spectra in the Nyquist and (c) Bode representations. Dots represent experimental points, while lines stand for fits to the equivalent circuit of item (a).

R_{trap} is the resistance that characterizes the trapping of charge carriers at the interface. This parameter is also related to parasite charge recombination at the interface [76]. j_{rec}, the current density of the recombination step, is a function of several microscopic parameters. Its expression is given by equation 3 [77,78]:

$$j_{rec} = q\,\sigma_{e^-}\,\upsilon_{e^-}\,n_{surf}\,p_{surf} \qquad \text{Equation (3)}$$

Where, j_{rec} is the recombination current density, q is the elemental charge, σ_{e^-} stands for the electrons' capture cross section while υ_{e^-} is the thermal velocity of electrons. The rate constant of the recombination process is given by $k_{rec} = \sigma_n \upsilon_n n_{surf}$ [77,79,80]. n_{surf} and

p_{surf} represent the electrons and holes trapped at the surface. Equation 3 is also helpful to explain the physical meaning of R_{trap} because it expresses that recombination (j_{rec}) is directly proportional to the amount of charges confined at the surface (n_{surf} and p_{surf}). This is why the trapping resistance R_{trap} is also a measure of charge recombination [76]. The lower the value of R_{trap}, the faster charge trapping is at the interface and hence the more important charge recombination is [81]. In the circuit of Figure 8-a, constant-phase elements have been added in order to account for surface heterogeneities and roughness. Constant phase elements (CPE) are commonly used to calculate the capacitance of non-ideal interfaces according to equation 4 [67]:

$$C = Q_0^{1/n} R_0^{(1-n)/n} \qquad \text{Equation (4)}$$

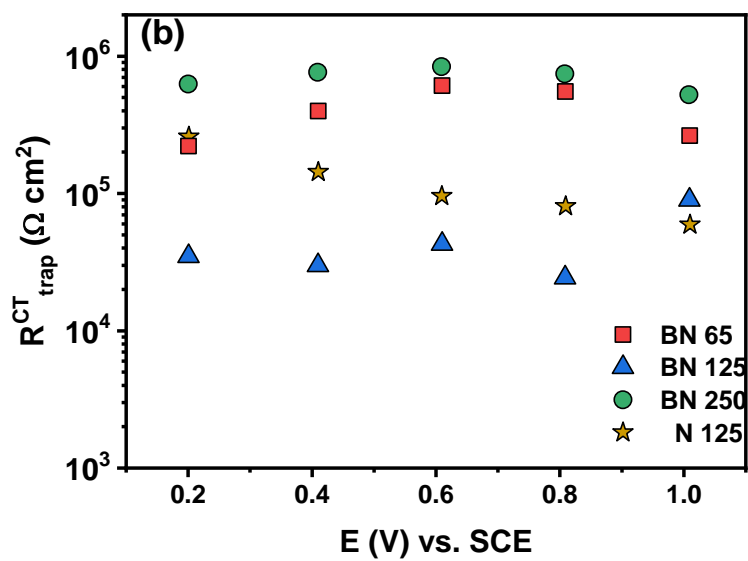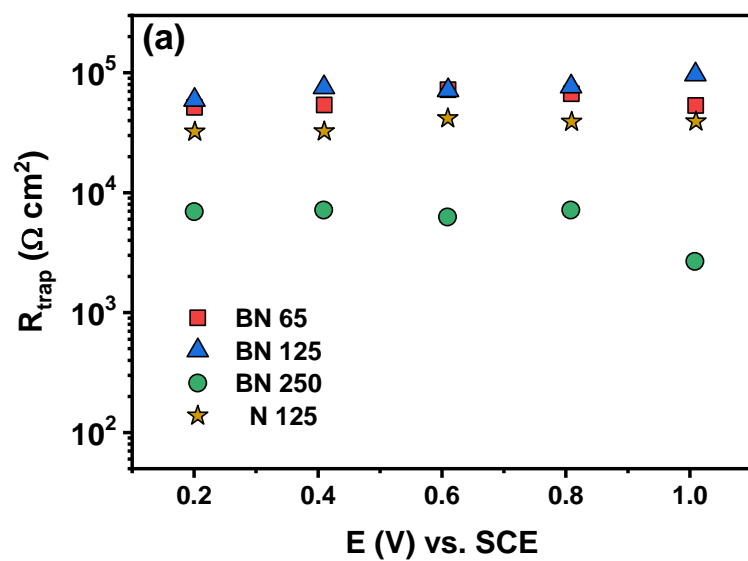Where n represents the exponent of the CPE.

When considering the different performance obtained using these photoelectrodes, it is worth noting that there are a large number of parameters that do influence the observed behavior, namely, oxygen vacancies, B/N incorporation in the TiO_2, lattice surface compositions, preferred crystal orientation, morphology and film thickness. Unfortunately, all these factors cannot be resolved by PEIS, and they are embodied in the interfacial resistances and capacitances derived from the analysis. Therefore, only a general discussion of the dynamic behavior during water splitting can be performed, always bearing in mind that all the factors simultaneously influence the measured photocurrent.

Typical PEIS spectra measured on each photoelectrode under the same light intensity (63 mW.cm^{-2}) and electrode potential (0.8 V/SCE) are shown in Figure 8-b and 8-c, in Nyquist and Bode representations, respectively. A good agreement was obtained between experimental and calculated PEIS diagrams. Results provide an explanation of the experimental trends observed on the photocurrents depicted in Figures 7-a and 7-b. For

example, the BN250 sample displayed the lowest photocurrent; this is the sample for which the lowest R_{trap} values were obtained (Figure 9-a), indicating a fast charge recombination rate, along with the largest R_{trap}^{CT} value (Figure 9-b), indicating a rather sluggish rate of hole transfer to the electrolyte. Such poor kinetics can be related to the long oxidizing/doping process, leading to a thick film where most photoexcited charge carriers are lost by recombination.

Regarding the other samples, the recombination resistance (R_{trap}) was found fairly similar over the potential range explored (Figure 9-a). However, a lower R_{trap}^{CT} value was obtained for the BN125 sample (Figure 9-b), indicating that the fastest charge transfer process occurred in this system, which displayed the highest photocurrent (Figure 7-a). This result suggests that this sample has the optimum characteristics, leading to the best compromise between charge transfer through the interface, and the surface recombination.

As expected, Mott-Schottky plots of the bulk capacitances measured on the different samples displayed linear behaviors (Figure 9-c). A flat-band potential, independent of the film thickness, was found at approximately -0.3 V/SCE. A plot of the trapping capacitances versus electrode potential is provided in Figure 9-d. The BN-250 sample presented the lowest values, in contrast to the BN-125 electrode which possessed the biggest trapping capacitance. The larger C_{trap} value was obtained in sample BN-125. This is likely to be due to the high surface density of minority carriers at the interface, which are then easily transferred to the electrolyte to split water. Likewise, the sample BN-250 had the lowest occupation of surface states with reactive intermediates, and this is an explanation for the small photocurrent shown in Figure 7-a.

(a)

R_{trap} (Ω cm^2)

E (V) vs. SCE

- ■ BN 65
- ▲ BN 125
- ● BN 250
- ★ N 125

(b)

R^{CT}_{trap} (Ω cm^2)

E (V) vs. SCE

- ■ BN 65
- ▲ BN 125
- ● BN 250
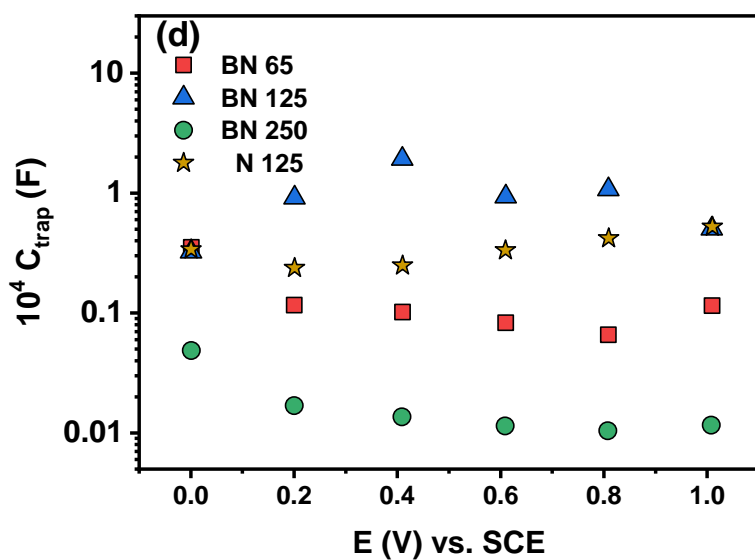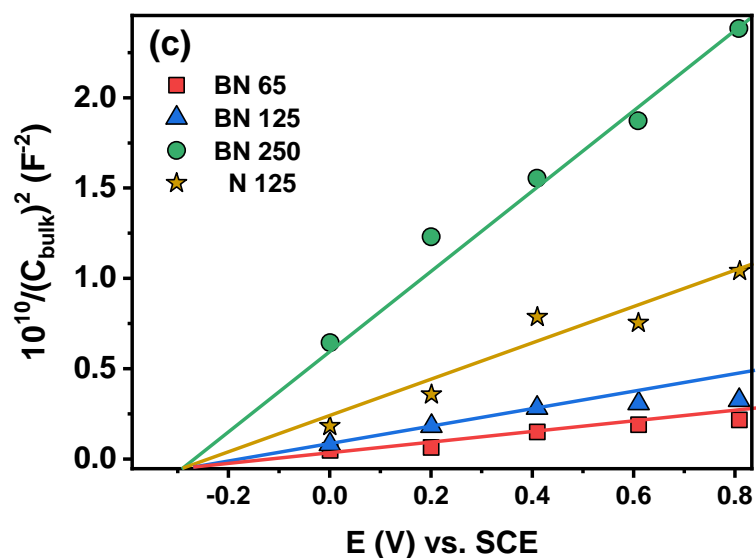- ★ N 125

Figure 9. Plots versus electrode potential of (a) the trapping resistance; (b) the charge transfer resistance from traps; (c) the bulk capacitance in Mott-Schottky coordinates and (d) trapping capacitance.

According to the results discussed above, the mechanism of the photoelectrochemical processes for B/N co-doped rutile [110] are illustrated in Figure 10. The impurities level of

oxygen vacancies, nitrogen and boron between valance band and conduction band enhanced the rutile activity under visible light. When the photoanode is excited with visible light, the electron and holes are generated and react with electrolyte. The transfer of photon-generated electrons to Ti-foil (back contact) and of photon-generated holes to the interface between electrode/electrolyte occurred. The holes were produced from boron, nitrogen and oxygen vacancies-induced new states just above and from valence band, which improves the water oxidation.
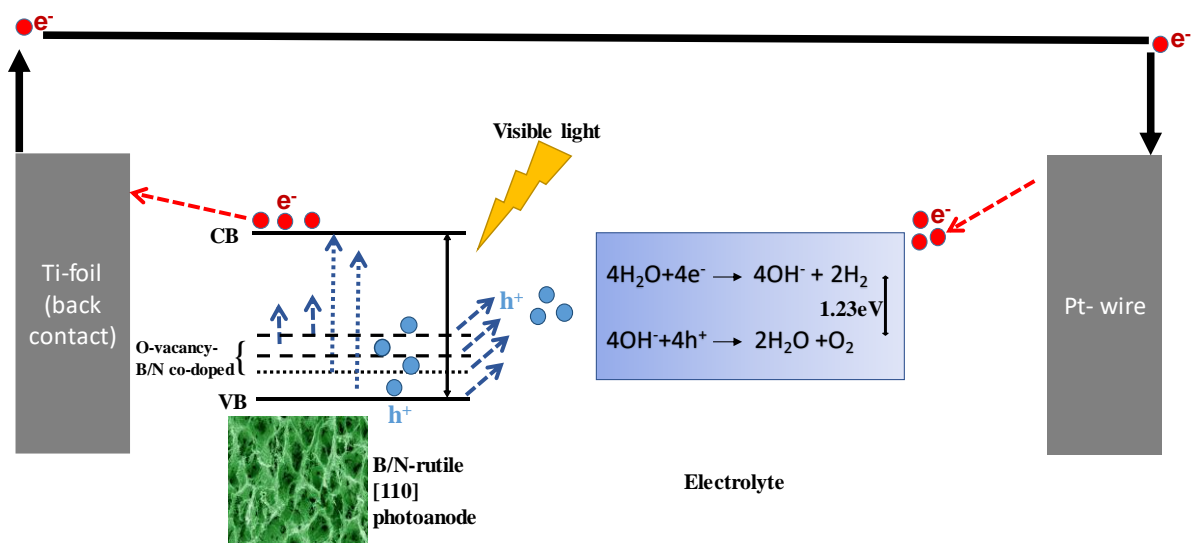
Figure 10. Schematic representation of excitations in BN125 photoanode under visible light.

Conclusion

In this work, we presented an innovated photocatalyst based on boron and nitrogen co-doped TiO_2 rutile (110) thin films. The samples have been prepared by simultaneously oxidizing and doping a Ti-foil substrate at 750°C. The formation of Ti-O-N and Ti-O-B-N bonds was demonstrated by X-ray photoelectron spectroscopy analysis. A honeycomb morphology has been put into evidence by Scanning Electron Microscopy, and the presence of crystal defects in the lattice has been revealed by Raman spectroscopy. UV−visible spectrophotometry has

been used to measure the visible light absorption properties of the material which have been attributed to the presence of oxygen vacancies and the introduction of impurity levels. Photo-Electrochemical Impedance Spectroscopy has been used to analyze the charge transfer mechanism. A model that takes into account the existence of surface trapping sites has been used to measure several microscopic rate parameters such as the trapping resistance and capacitance, the charge transfer resistance and the bulk capacitances. The values of these different parameters have been measured over the 0.0/1.0 V/SCE potential range, and a stable and high photocurrent activity up to 270 $\mu A/cm^2$ under visible light has been obtained for the BN125 sample. The results presented in this work open new prospects for TiO_2 nanomaterials synthesis and for the photocatalysis community.

References

[1]   A.A. Nada, M.F. Bekheet, R. Viter, P. Miele, S. Roualdes, M. Bechelany, BN/GdxTi (1-x) O (4-x)/2 nanofibers for enhanced photocatalytic hydrogen production under visible light, Appl. Catal. B Environ. 251 (2019) 76–86. doi:10.1016/j.apcatb.2019.03.043.

[2]   O. Diwald, T.L. Thompson, T. Zubkov, E.G. Goralski, S.D. Walck, J.T. Yates, Photochemical activity of nitrogen-doped rutile TiO2 (110) in visible light, J. Phys. Chem. B. 108 (2004) 6004–6008.

[3]   L. Li, Z. Qin, L. Ries, S. Hong, T. Michel, J. Yang, C. Salameh, M. Bechelany, P. Miele, D. Kaplan, Role of Sulfur Vacancies and Undercoordinated Mo Regions in MoS2 Nanosheets Towards the Evolution of Hydrogen, ACS Nano. (2019).

[4]   Q. Zeng, J. Bai, J. Li, B. Zhou, Y. Sun, A low-cost photoelectrochemical tandem cell for highly-stable and efficient solar water splitting, Nano Energy. 41 (2017) 225–232.

[5] P. Wu, Z. Liu, D. Chen, M. Zhou, J. Wei, Flake-like NiO/WO₃ p-n heterojunction photocathode for photoelectrochemical water splitting, Appl. Surf. Sci. 440 (2018) 1101–1106. doi:10.1016/j.apsusc.2018.01.292.

[6] H.H. El-maghrabi, A. Barhoum, A.A. Nada, Y. Mohamed, S. Mikhail, A.M. Youssef, Synthesis of mesoporous core-shell CdS@TiO2 (0D and 1D) photocatalysts for solar-driven hydrogen fuel production, "Journal Photochem. Photobiol. A Chem. 351 (2018) 261–270. doi:10.1016/j.jphotochem.2017.10.048.

[7] J. Deng, X. Lv, J. Zhong, Photocharged Fe2TiO5/Fe2O3 Photoanode for Enhanced Photoelectrochemical Water Oxidation, J. Phys. Chem. C. 122 (2018) 29268–29273.

[8] A.A. Nada, M. Nasr, R. Viter, P. Miele, S. Roualdes, M. Bechelany, Mesoporous ZnFe2O4@TiO2nanofibers prepared by electrospinning coupled to PECVD as highly performing photocatalytic materials, J. Phys. Chem. C. (2017). doi:10.1021/acs.jpcc.7b08567.

[9] H.H. El-Maghrabi, E.A. Nada, F.S. Soliman, Y.M. Moustafa, A.E.-S. Amin, One pot environmental friendly nanocomposite synthesis of novel TiO2-nanotubes on graphene sheets as effective photocatalyst, Egypt. J. Pet. 25 (2016) 575–584.

[10] W.M.A. El Rouby, A.A. Farghali, Titania morphologies modified gold nanoparticles for highly catalytic photoelectrochemical water splitting, J. Photochem. Photobiol. A Chem. 364 (2018) 740–749. doi:10.1016/j.jphotochem.2018.07.011.

[11] E. Safaei, S. Mohebbi, M. Irani, Selective aerobic photocatalytic oxidation of benzyl alcohol over spherical structured WO 3/TiO 2 nanocomposite under visible light irradiation, J. Sol-Gel Sci. Technol. 87 (2018) 170–182.

[12] J. Gou, Q. Ma, X. Deng, Y. Cui, H. Zhang, X. Cheng, X. Li, M. Xie, Q. Cheng,

Fabrication of Ag2O/TiO2-Zeolite composite and its enhanced solar light photocatalytic performance and mechanism for degradation of norfloxacin, Chem. Eng. J. 308 (2017) 818–826.

[13]   R.A. Sayed, S.E. Abd El Hafiz, N. Gamal, Y. GadelHak, W.M.A. El Rouby, Co-Fe layered double hydroxide decorated titanate nanowires for overall photoelectrochemical water splitting, J. Alloys Compd. 728 (2017) 1171–1179. doi:10.1016/j.jallcom.2017.09.083.

[14]   M. Antuch, W.M.A. El Rouby, P. Millet, A comparison of water photo-oxidation and photo-reduction using photoelectrodes surface-modified by deposition of co-catalysts: Insights from photo-electrochemical impedance spectroscopy, Int. J. Hydrogen Energy. (2018). doi:10.1016/j.ijhydene.2018.11.214.

[15]   Y. GadelHak, W.M.A. El Rouby, A.A. Farghali, Au-decorated 3D/1D titanium dioxide flower-like/rod bilayers for photoelectrochemical water oxidation, Electrochim. Acta. 306 (2019) 185–197. doi:10.1016/j.electacta.2019.03.118.

[16]   X. Wang, T. Li, R. Yu, H. Yu, J. Yu, Highly efficient TiO 2 single-crystal photocatalyst with spatially separated Ag and F− bi-cocatalysts: orientation transfer of photogenerated charges and their rapid interfacial reaction, J. Mater. Chem. A. 4 (2016) 8682–8689.

[17]   N. Ahmed, M. Ramadan, W.M.A. El Rouby, A.A. Farghali, N.K. Allam, Non-precious co-catalysts boost the performance of TiO2 hierarchical hollow mesoporous spheres in solar fuel cells, Int. J. Hydrogen Energy. 43 (2018) 21219–21230. doi:10.1016/j.ijhydene.2018.10.012.

[18]   A. Merenda, M. Weber, M. Bechelany, F.-M. Allioux, L. Hyde, L. Kong, L.F. Dumée, Fabrication of Pd-TiO2 nanotube photoactive junctions via Atomic Layer Deposition

for persistent pesticide pollutants degradation, Appl. Surf. Sci. 483 (2019) 219–230.

[19]   D. Dvoranová, V. Brezová, M. Mazúr, M.A. Malati, Investigations of metal-doped titanium dioxide photocatalysts, Appl. Catal. B Environ. 37 (2002) 91–105. doi:https://doi.org/10.1016/S0926-3373(01)00335-6.

[20]   H.H. El-Maghrabi, A.A. Nada, K.R. Diab, A.M. Youssef, A. Hamdy, S. Roualdes, S. Abd El-Wahab, Facile fabrication of NiTiO$_3$/graphene nanocomposites for photocatalytic hydrogen generation, J. Photochem. Photobiol. A Chem. 365 (2018). doi:10.1016/j.jphotochem.2018.07.040.

[21]   W.M.A. El Rouby, Selective adsorption and degradation of organic pollutants over Au decorated Co doped titanate nanotubes under simulated solar light irradiation, J. Taiwan Inst. Chem. Eng. 88 (2018) 201–214. doi:10.1016/j.jtice.2018.04.003.

[22]   M. Janus, B. Tryba, M. Inagaki, A.W. Morawski, New preparation of a carbon-TiO2 photocatalyst by carbonization of n-hexane deposited on TiO2, Appl. Catal. B Environ. 52 (2004) 61–67. doi:https://doi.org/10.1016/j.apcatb.2004.03.011.

[23]   Y. Li, G. Ma, S. Peng, G. Lu, S. Li, Boron and nitrogen co-doped titania with enhanced visible-light photocatalytic activity for hydrogen evolution, Appl. Surf. Sci. 254 (2008) 6831–6836. doi:https://doi.org/10.1016/j.apsusc.2008.04.075.

[24]   M.H. Elbakkay, W.M.A. El Rouby, S.I. El-Dek, A.A. Farghali, S-TiO2/S-reduced graphene oxide for enhanced photoelectrochemical water splitting, Appl. Surf. Sci. 439 (2018) 1088–1102. doi:10.1016/j.apsusc.2018.01.070.

[25]   A. Mittal, B. Mari, S. Sharma, V. Kumari, S. Maken, K. Kumari, Non-metal modified TiO2: a step towards visible light photocatalysis, J. Mater. Sci. Mater. Electron. 0 (2019) 0. doi:10.1007/s10854-018-00651-9.

[26] M. Weber, N. Tuleushova, J. Zgheib, C. Lamboux, I. Iatsunskyi, E. Coy, V. Flaud, S. Tingry, D. Cornu, P. Miele, Enhanced electrocatalytic performance triggered by atomically bridged boron nitride between palladium nanoparticles and carbon fibers in gas-diffusion electrodes, Appl. Catal. B Environ. 257 (2019) 117917.

[27] M. Weber, J.-Y. Kim, J.-H. Lee, J.-H. Kim, I. Iatsunskyi, E. Coy, P. Miele, M. Bechelany, S.S. Kim, Highly efficient hydrogen sensors based on Pd nanoparticles supported on boron nitride coated ZnO nanowires, J. Mater. Chem. A. 7 (2019) 8107–8116.

[28] C. Haisch, C. Günnemann, S. Melchers, M. Fleisch, J. Schneider, A. V Emeline, D.W. Bahnemann, Irreversible surface changes upon n-type doping – A photoelectrochemical study on rutile single crystals, Electrochim. Acta. 280 (2018) 278–289. doi:https://doi.org/10.1016/j.electacta.2018.05.105.

[29] X. Wang, W. Wang, X. Wang, J. Zhang, J. Zhao, Z. Gu, L. Zhou, structural characterization and evaluation of floating B-N codoped TiO 2 / expanded perlite composites with enhanced visible light photoactivity, Appl. Surf. Sci. 349 (2015) 264–271. doi:10.1016/j.apsusc.2015.05.002.

[30] M.-Y. Xing, W.-K. Li, Y.-M. Wu, J.-L. Zhang, X.-Q. Gong, Formation of new structures and their synergistic effects in boron and nitrogen codoped TiO2 for enhancement of photocatalytic performance, J. Phys. Chem. C. 115 (2011) 7858–7865.

[31] K. Zhang, X. Wang, T. He, X. Guo, Y. Feng, Preparation and photocatalytic activity of B – N co-doped mesoporous TiO 2, Powder Technol. 253 (2014) 608–613. doi:10.1016/j.powtec.2013.12.024.

[32] H. Xue, Y. Jiang, K. Yuan, T. Yang, J. Hou, C. Cao, Floating photocatalyst of B – N – TiO 2 / expanded perlite : a sol – gel synthesis with optimized mesoporous and high

photocatalytic activity, Nat. Publ. Gr. (2016) 2–10. doi:10.1038/srep29902.

[33]   J. Yuan, E. Wang, Y. Chen, W. Yang, J. Yao, Y. Cao, Doping mode , band structure
       and photocatalytic mechanism of B – N-codoped, Appl. Surf. Sci. 257 (2011) 7335–
       7342. doi:10.1016/j.apsusc.2011.03.139.

[34]   J. Zhao, L. Zhang, W. Xing, K. Lu, A Novel Method To Prepare B / N Codoped
       Anatase TiO 2, (2015). doi:10.1021/jp512837n.

[35]   X. Lin, D. Fu, Facile one-pot hydrothermal synthesis of B / N-codoped TiO 2 hollow
       spheres with enhanced visible-light photocatalytic activity and photoelectrochemical
       property, Solid State Sci. 34 (2014) 73–77.
       doi:10.1016/j.solidstatesciences.2014.05.007.

[36]   X. Zhou, F. Peng, H. Wang, H. Yu, J. Yang, Effect of nitrogen-doping temperature on
       the structure and photocatalytic activity of the B , N-doped TiO 2, J. Solid State Chem.
       184 (2011) 134–140. doi:10.1016/j.jssc.2010.10.039.

[37]   X. Ding, X. Song, P. Li, Z. Ai, L. Zhang, Efficient visible light driven photocatalytic
       removal of NO with aerosol flow synthesized B , N-codoped TiO 2 hollow spheres, J.
       Hazard. Mater. 190 (2011) 604–612. doi:10.1016/j.jhazmat.2011.03.099.

[38]   M. Weber, E. Coy, I. Iatsunskyi, L. Yate, P. Miele, M. Bechelany, Mechanical
       properties of boron nitride thin films prepared by atomic layer deposition,
       CrystEngComm. 19 (2017) 6089–6094.

[39]   J. Rodríguez-Carvajal, Recent Developments of the Program FULLPROF, Comm.
       Powder Diffr. 26 (2001) 12–19.

[40]   L.W. Finger, D.E. Cox, A.P. Jephcoat, A Correction for powder diffraction peak
       asymmetry due to axial divergence, J. Appl. Crystallogr. 27 (1994) 892–900.

doi:10.1107/S0021889894004218.

[41]   A. Fajar, E. Kartini, H. Mugirahardjo, M. Ihsan, Crystallite Size and Microstrain
       Measurement of Cathode Material after Mechanical Milling using Neutron Diffraction
       Technique, Atom Indones. 36 (2010) 111–115.
       http://download.portalgaruda.org/article.php?article=51561&val=4151.

[42]   W.A. Dollase, Correction of intensities for preferred orientation in powder
       diffractometry: application of the March model, J. Appl. Crystallogr. 19 (1986) 267–
       272.

[43]   E. Zolotoyabko, Determination of the degree of preferred orientation within the
       March–Dollase approach, J. Appl. Crystallogr. 42 (2009) 513–518.

[44]   H. Perron, C. Domain, J. Roques, R. Drot, E. Simoni, H. Catalette, Optimisation of
       accurate rutile TiO_2 (110),(100),(101) and (001) surface models from periodic DFT
       calculations, Theor. Chem. Acc. 117 (2007) 565–574.

[45]   A. Howard, C.E.J. Mitchell, D. Morris, R.G. Egdell, S.C. Parker, The surface structure
       of TiO_2 (210) studied by atomically resolved STM and atomistic simulation, Surf. Sci.
       448 (2000) 131–141.

[46]   U. Diebold, The surface science of titanium dioxide, Surf. Sci. Rep. 48 (2003) 53–229.

[47]   L. Meng, H. Chen, C. Li, M.P. Dos Santos, Growth of the [110] oriented TiO_2
       nanorods on ITO substrates by sputtering technique for dye-sensitized solar cells,
       Front. Mater. 1 (2014) 14.

[48]   C. V Thompson, Structure evolution during processing of polycrystalline films, Annu.
       Rev. Mater. Sci. 30 (2000) 159–190.

[49]   R.G. Palgrave, D.J. Payne, R.G. Egdell, Nitrogen diffusion in doped TiO_2 (110)

single crystals: a combined XPS and SIMS study, J. Mater. Chem. 19 (2009) 8418–8425.

[50] X. Zhou, F. Peng, H. Wang, H. Yu, J. Yang, Preparation of B, N-codoped nanotube arrays and their enhanced visible light photoelectrochemical performances, Electrochem. Commun. 13 (2011) 121–124.

[51] J.-H. Lee, J.-I. Youn, Y.-J. Kim, I.-K. Kim, K.-W. Jang, H.-J. Oh, Photocatalytic characteristics of boron and nitrogen doped titania film synthesized by micro-arc oxidation, Ceram. Int. 41 (2015) 11899–11907.

[52] T. Hirata, Pressure, temperature and concentration dependences of phonon frequency with variable Grüneisen parameter: Fits to the Raman-active Eg mode in TiO_2 and $Ti_{1-x}Zr_xO_2$ ($X \leq 0.1$), Phys. Status Solidi Basic Res. 209 (1998) 17–24. doi:10.1002/(SICI)1521-3951(199809)209:1<17::AID-PSSB17>3.0.CO;2-R.

[53] V. Gombac, L. De Rogatis, A. Gasparotto, G. Vicario, T. Montini, D. Barreca, G. Balducci, P. Fornasiero, E. Tondello, M. Graziani, TiO2 nanopowders doped with boron and nitrogen for photocatalytic applications, Chem. Phys. 339 (2007) 111–123.

[54] X. Zhou, F. Peng, H. Wang, H. Yu, Boron and nitrogen-codoped TiO2 nanorods: Synthesis, characterization, and photoelectrochemical properties, J. Solid State Chem. 184 (2011) 3002–3007.

[55] S.R. Joshi, B. Padmanabhan, A. Chanda, I. Mishra, V.K. Malik, N.C. Mishra, D. Kanjilal, S. Varma, Optical studies of cobalt implanted rutile TiO2 (110) surfaces, Appl. Surf. Sci. 387 (2016) 938–943. doi:https://doi.org/10.1016/j.apsusc.2016.07.038.

[56] Y. Fang, X. Kong, D. Wang, S. Cui, J. Liu, Role of dopant Ga in tuning the band gap of rutile TiO2 from first principles, Chinese J. Phys. 56 (2018) 1370–1377.

doi:https://doi.org/10.1016/j.cjph.2018.04.011.

[57]   S.A. Ansari, M.M. Khan, M.O. Ansari, M.H. Cho, Nitrogen-doped titanium dioxide
        (N-doped TiO 2) for visible light photocatalysis, New J. Chem. 40 (2016) 3000–3009.

[58]   S.S. Surah, M. Vishwakarma, R. Kumar, R. Nain, S. Sirohi, G. Kumar, Tuning the
        electronic band alignment properties of TiO2 nanotubes by boron doping, Results
        Phys. 12 (2019) 1725–1731.

[59]   G.R. Torres, T. Lindgren, J. Lu, C.-G. Granqvist, S.-E. Lindquist,
        Photoelectrochemical Study of Nitrogen-Doped Titanium Dioxide for Water
        Oxidation, J. Phys. Chem. B. 108 (2004) 5995–6003. doi:10.1021/jp037477s.

[60]   G. Yan, M. Zhang, J. Hou, J. Yang, Photoelectrochemical and photocatalytic
        properties of N+ S co-doped TiO2 nanotube array films under visible light irradiation,
        Mater. Chem. Phys. 129 (2011) 553–557.

[61]   N. Lu, X. Quan, J. Li, S. Chen, H. Yu, G. Chen, Fabrication of boron-doped TiO2
        nanotube array electrode and investigation of its photoelectrochemical capability, J.
        Phys. Chem. C. 111 (2007) 11836–11842.

[62]   J. Li, N. Lu, X. Quan, S. Chen, H. Zhao, Facile Method for Fabricating Boron-Doped
        TiO2 Nanotube Array with Enhanced Photoelectrocatalytic Properties, Ind. Eng.
        Chem. Res. 47 (2008) 3804–3808. doi:10.1021/ie0712028.

[63]   M. Antuch, P. Millet, A. Iwase, A. Kudo, S.A. Grigoriev, Y.Z. Voloshin,
        Characterization of Rh:SrTiO3 photoelectrodes surface-modified with a cobalt
        clathrochelate and their application to the hydrogen evolution reaction, Electrochim.
        Acta. 258 (2017) 255–265. doi:10.1016/j.electacta.2017.10.018.

[64]   M. Antuch, W.M.A. El Rouby, P. Millet, A comparison of water photo-oxidation and

photo-reduction using photoelectrodes surface-modified by deposition of co-catalysts : Insights from photo-electrochemical impedance spectroscopy, Int. J. Hydrogen Energy. 44 (2019) 9970–9977. doi:10.1016/j.ijhydene.2018.11.214.

[65] M. Antuch, P. Millet, A. Iwase, A. Kudo, Water reduction into hydrogen using Rh-doped SrTiO3 photoelectrodes surface-modified by minute amounts of Pt: Insights from heterogeneous kinetic analysis, Electrochim. Acta. 297 (2019) 696–704. doi:10.1016/j.electacta.2018.11.110.

[66] A. Liu, Y. Zhang, W. Ma, W. Song, C. Chen, J. Zhao, Facial boron incorporation in hematite photoanode for enhanced photoelectrochemical water oxidation, J. Photochem. Photobiol. A Chem. 355 (2017) 290–297. doi:10.1016/j.jphotochem.2017.08.045.

[67] F.E. Bedoya-Lora, A. Hankin, I. Holmes-Gentle, A. Regoutz, M. Nania, D.J. Payne, J.T. Cabral, G.H. Kelsall, Effects of low temperature annealing on the photo-electrochemical performance of tin-doped hematite photo-anodes, Electrochim. Acta. 251 (2017) 1–11. doi:10.1016/j.electacta.2017.08.090.

[68] S. Jamali, A. Moshaii, Improving photo-stability and charge transport properties of Cu2O/CuO for photo-electrochemical water splitting using alternate layers of WO3or CuWO4produced by the same route, Appl. Surf. Sci. 419 (2017) 269–276. doi:10.1016/j.apsusc.2017.04.228.

[69] S.Y. Lim, D. Han, Y.R. Kim, T.D. Chung, Photoelectrochemical and Impedance Spectroscopic Analysis of Amorphous Si for Light-Guided Electrodeposition and Hydrogen Evolution Reaction, ACS Appl. Mater. Interfaces. 9 (2017) 23698–23706. doi:10.1021/acsami.7b04961.

[70] H. Hajibabaei, A.R. Schon, T.W. Hamann, Interface Control of Photoelectrochemical

Water Oxidation Performance with Ni 1– x Fe x O y Modified Hematite Photoanodes, Chem. Mater. 29 (2017) acs.chemmater.7b01149. doi:10.1021/acs.chemmater.7b01149.

[71] O. Zandi, A.R. Schon, H. Hajibabaei, T.W. Hamann, Enhanced Charge Separation and Collection in High-Performance Electrodeposited Hematite Films, Chem. Mater. 28 (2016) 765–771. doi:10.1021/acs.chemmater.5b03707.

[72] P. Dias, L. Andrade, A. Mendes, Hematite-based photoelectrode for solar water splitting with very high photovoltage, Nano Energy. 38 (2017) 218–231. doi:10.1016/j.nanoen.2017.05.051.

[73] C. Miao, T. Shi, G. Xu, S. Ji, C. Ye, Photocurrent enhancement for Ti-doped Fe2O3thin film photoanodes by an in situ solid-state reaction method, ACS Appl. Mater. Interfaces. 5 (2013) 1310–1316. doi:10.1021/am302575p.

[74] S. Hernández, G. Gerardi, K. Bejtka, A. Fina, N. Russo, Environmental Evaluation of the charge transfer kinetics of spin-coated BiVO4 thin films for sun-driven water photoelectrolysis, Appl. Catal. B Environ. 190 (2016) 66–74. doi:10.1016/j.apcatb.2016.02.059.

[75] K.J. Pyper, J.E. Yourey, B.M. Bartlett, Reactivity of CuWO4 in photoelectrochemical water oxidation is dictated by a midgap electronic state, J. Phys. Chem. C. 117 (2013) 24726–24732. doi:10.1021/jp408434v.

[76] S.C. Riha, B.M. Klahr, E.C. Tyo, S. Seifert, S. Vajda, M.J. Pellin, T.W. Hamann, A.B.F. Martinson, Atomic layer deposition of a submonolayer catalyst for the enhanced photoelectrochemical performance of water oxidation with hematite, ACS Nano. 7 (2013) 2396–2405. doi:10.1021/nn305639z.

[77] H.-J. Lewerenz, L. Peter, Photoelectrochemical Water Splitting Materials, Processes and Architectures, RSC Publishing, 2013.

[78] A.J. Bard, L.R. Faulkner, Electrochemical Methods Fundamentals and Applications, 2nd ed., John Wiley & Sons, Inc., 2001.

[79] D.J. Fermín, E.A. Ponomarev, L.M. Peter, Kinetic study of CdS photocorrosion by intensity modulated photocurrent and photoelectrochemical impedance spectroscopy, J. Electroanal. Chem. 473 (1999) 192–203. doi:10.1016/S0022-0728(99)00109-6.

[80] W.H. Leng, Z. Zhang, J.Q. Zhang, C.N. Cao, Investigation of the Kinetics of a TiO2 Photoelectrocatalytic Reaction Involving Charge Transfer and Recombination through Surface States by Electrochemical Impedance Spectroscopy, J. Phys. Chem. B. 109 (2005) 15008–15023. doi:10.1021/jp051821z.

[81] F. Fabregat-santiago, G. Garcia-Belmonte, I. Mora-Sero, J. Bisquert, Characterization of nanostructured hybrid and organic solar cells by impedance spectroscopy, Phys. Chem. Chem. Phys. 13 (2011) 9083–9118. doi:10.1039/c0cp02249g.